

# Distributed finite element solution using model order reduction\*

Tom Gustafsson<sup>a</sup>, Antti Hannukainen<sup>b</sup>, Vili Kohonen<sup>b</sup>

<sup>a</sup>*Department of Mechanical Engineering, Aalto University, P.O. Box 11100 00076  
Aalto, Espoo, Finland*

<sup>b</sup>*Department of Mathematics and Systems Analysis, Aalto University,*

---

## Abstract

We extend a localized model order reduction method for the distributed finite element solution of elliptic boundary value problems in the cloud. We give a computationally efficient technique to compute the required inner product matrices and optimal reduced bases. A memory-efficient methodology is proposed to project the global finite element linear system onto the reduced basis. Our numerical results demonstrate the technique using non-trivial tetrahedral meshes and subdomain interfaces with up to 85 million degrees-of-freedom on a laptop computer by distributing the bulk of the model order reduction to the cloud.

*Keywords:* finite element method, partial differential equations, model order reduction, distributed computing, cloud computing

*2020 MSC:* 65F55, 65N30, 65N55, 65Y05

---

## 1. Introduction

High performance computing (HPC) is often done using supercomputers that have fast internal networking. There is a focus on networking because the bottleneck in many HPC workloads can be traced back to message passing and sharing of data between the processes. Consequently, many distributed workloads benefit from specialized networking technologies or topologies that

---

\*This work was supported by the Academy of Finland (Decision 353080)

*Email addresses:* [tom.gustafsson@aalto.fi](mailto:tom.gustafsson@aalto.fi) (Tom Gustafsson),  
[antti.hannukainen@aalto.fi](mailto:antti.hannukainen@aalto.fi) (Antti Hannukainen), [vili.kohonen@aalto.fi](mailto:vili.kohonen@aalto.fi) (Vili Kohonen)

improve the node-to-node bandwidth and latency; see, e.g., [29]. Cloud computing, on the other hand, is a paradigm for resource allocation in data centers which relies on the virtualization technology. Commercial cloud capacity is ubiquitous, and the use of excess capacity can be cost-effective as many providers support a spot pricing model [22]. However, cloud services have different priorities than supercomputers when it comes to energy efficiency, security and networking. As a consequence, cloud computing may be more suitable for tasks with lower requirements for interprocess communication [8].

This study focuses on a distributed finite element solution technique for elliptic problems, proposed in [1], which eliminates the need for message passing during the solution of the linear system. The domain is decomposed into several overlapping subdomains as a preprocessing step and a local reduced basis is computed for each subdomain in parallel using randomized model order reduction techniques [6]. The basis reduction step is an embarrassingly parallel batch job that is suitable for any cluster of networked computing nodes, including virtual cloud instances. Because of no interprocess communication during the reduction, the bulk of the computation can be done out-of-order or on cheaper spot instances that may be interrupted at a moment's notice. This is in contrast to many of the traditional iterative solvers based on domain decomposition; see, e.g., [28, 26, 9]. From a practical perspective, the technique can be thought of as a more accurate alternative to the classical component mode synthesis techniques [24] that are based on non-overlapping subdomains.

After constructing the local bases in parallel, we are then able to greatly decrease the size of the finite element system matrix and improve its conditioning by projecting it onto the reduced basis. A majority of the computational work can be distributed and only one layer of interface elements must be assembled by the master node where an interpolation technique, a slight variation of the original partition of unity method [2], is used to match the bases originating from the different subdomains. The global error introduced by the reduction can be successfully controlled in the  $H^1$  norm through a parameter which specifies the maximum tolerance for the local relative error in each subdomain. The final reduced linear system can be solved using traditional techniques such as the conjugate gradient method on the master node or, as in our case, on a laptop computer.

The basis reduction is performed using a model order reduction technique that has been first introduced in the context of multiscale modelling [1, 3, 4]. The problem domain is partitioned and the subdomains extended to form

an overlap – the setup is reminiscent of the classical alternating Schwarz domain decomposition method [28]. In multiscale modelling, the extended subdomains are referred to as oversampling domains [11] and an optimal reduced basis can be constructed by finding and restricting the spectrum of a harmonic extension from the boundary of each extended subdomain. We note that the harmonic extension is close to some of the lifting operators used in the iterative domain decomposition literature; cf. [26]. In the context of multiscale modelling, we track the utilization of the oversampling domain trace space back to [10, 11]. However, our interest is purely the scaling of the methodology for large-scale computing.

In this study, we solve the elliptic source problem in a cloud computing environment and further optimize the computation through the use of randomized linear algebra [14, 21], which was applied to model order reduction in [7] and later in [6, 25]. A technique similar to ours was used for the distributed solution of the Laplace eigenvalue problem in [15]. The reduced bases from the local approximation spaces have been shown to be optimal in the sense of Kolmogorov  $n$ -width [1]. Precisely, the local approximation error converges exponentially with respect to the dimension of the local approximation space. Slightly tighter error bounds were derived in [20] for cuboidal domains, where the rate of convergence was also studied with respect to the sizes of the subdomain and its extension. Intuitively speaking, the rate increases with larger subdomain extensions.

Further, [19] analyzed the discrete problem, showing similar exponential convergence rates in the finite-dimensional setting and convergence to the continuous problem as  $h \rightarrow 0$ . Our work extends the theoretical discrete results. Some eigenvalue problem bounds were derived in terms of  $\ell_2$  norms in [7] whereas here we generate the local reduced bases from low-rank matrix approximations in the weighted  $\ell_2$  matrix norm. The approach is similar to [6, 25] with the difference that we show how to construct the required inner product matrices for properly weighted local norms, and compute the local approximation bases using them so that the matrix norms and the continuous  $H^1$  norms coincide. Convergence to the traditional finite element solution is immediate and the error or, alternatively, the size of the reduced basis, can be controlled easily using a single parameter.

While the existing literature on local approximation spaces often mentions the embarrassingly parallel nature of the basis creation, only [15], focusing on the Laplace eigenvalue problem, has previously included larger numerical examples with unstructured meshes and up to 10 million degrees-of-freedom

on a cluster of workstations. For very large problems, there are three main challenges that complicate or even prohibit scaling. First, naively computing the local inner product matrices required for constructing the reduced bases in the proper norm is expensive. We show how to do this efficiently without forming the local Schur complement. Second, the local reduced bases need to be as small as possible to create a compact global transformation. Computing the basis with an explicit SVD is costly and using plain sketching from randomized linear algebra [21], while fast, introduces lots of redundant dimensions to the basis. We outline a variant of randomized SVD that produces almost optimal local bases with very high probability while being practically as fast as the sketching-only routine. Third, the transformation of the original system to the reduced basis requires prohibitive amounts of memory if done naively. We propose a memory-efficient methodology to do the projection such that laptop memory suffices. With these optimizations, the method can be scaled to very large problems in three dimensions.

We focus on the Poisson source problem and compute three-dimensional numerical examples with up to 85 million degrees-of-freedom on a laptop computer by distributing the bulk of the model order reduction to the cloud. The method enables large-scale computing in a publicly available massively parallel computing environment. Unlike most studies that concentrate on structured and regular grid-like mesh partitions and extensions, we experiment with arbitrary partitions obtained via graph partitioning tools. Contrary to the remarks of other authors [7, 6, 25], the scaling of the local problems with respect to the number of degrees-of-freedom on the boundary of the extended subdomain is not an issue in the distributed setting even when explicitly creating the lifting operator and finding its singular values. For extended subdomains with 10 000–20 000 nodes, the local problems take around a minute to solve for our explicit solver. Randomized numerical linear algebra is used to cut down the solution times to seconds for the same local problems, although in principle to a lessened degree of error control. In practice, the combination of the slack local error estimate and the tight probabilistic bounds given, e.g., in [14] causes us to observe practically identical results with the explicit and the randomized variant.

The rest of the paper is organized as follows. In section 2, we introduce the elliptic model problem and its (approximate) discrete formulation. Next, we give a high-level presentation of the domain decomposition method in section 3. Section 4 follows with an analysis how to approximate the harmonic extension operator in proper norms. In section 5, we derive a global error

estimate for the reduced basis approximation. Then, we discuss implementational details in section 6. Section 7 closes off with numerical error and scaling tests.

## 2. Model problem

Let  $\Omega \subset \mathbb{R}^d$ ,  $d \in \{2, 3\}$ , be a polygonal/polyhedral domain and  $f \in L^2(\Omega)$ . We consider the boundary value problem: find  $\phi$  such that

$$\begin{aligned} -\Delta\phi &= f && \text{in } \Omega, \\ \phi &= 0 && \text{on } \partial\Omega. \end{aligned} \tag{2.1}$$

The finite element method is based on the weak formulation of the above problem. We analyze (2.1) to retain our focus in developing an efficient numerical method. More general problems in terms of parameterization and boundary conditions have been studied in [1, 3, 4].

**Problem 2.1** (Continuous formulation). Find  $\phi \in H_0^1(\Omega)$  such that

$$\int_{\Omega} \nabla\phi \cdot \nabla v \, dx = \int_{\Omega} f v \, dx \quad \forall v \in H_0^1(\Omega), \tag{2.2}$$

where  $f \in L^2(\Omega)$ .

We introduce a shape-regular finite element triangulation/tetrahedralization  $\mathcal{T}$ , of maximum diameter  $h$ , and the corresponding space of continuous, piecewise linear finite elements  $V \subset H_0^1(\Omega)$ . The discrete weak formulation corresponding to (2.2) is obtained by replacing  $H_0^1(\Omega)$  with its finite-dimensional counterpart.

**Problem 2.2** (Discrete formulation). Find  $u \in V$  such that

$$\int_{\Omega} \nabla u \cdot \nabla v \, dx = \int_{\Omega} f v \, dx \quad \forall v \in V. \tag{2.3}$$

The number of elements in  $\mathcal{T}$  is assumed to be large enough for the direct solution of (2.3) to be unfeasible. In the next section, we construct a reduced space  $\tilde{V} \subset V$  so that  $\dim \tilde{V} \ll \dim V$ .

**Problem 2.3** (Reduced discrete formulation). Find  $\tilde{u} \in \tilde{V}$  such that

$$\int_{\Omega} \nabla \tilde{u} \cdot \nabla v \, dx = \int_{\Omega} f v \, dx \quad \forall v \in \tilde{V}. \tag{2.4}$$

In the rest of the paper, we use the following standard notation for the  $L^2$  and  $H^1$  norms over  $S \subset \Omega$ , respectively:

$$\|w\|_{0,S}^2 = \int_S w^2 dx, \quad \|w\|_{1,S}^2 = \|w\|_{0,S}^2 + \|\nabla w\|_{0,S}^2.$$

### 3. Domain decomposition

The domain  $\Omega$  is split into  $n$  overlapping subdomains  $\Omega = \omega_1 \cup \dots \cup \omega_n$  so that the boundaries  $\partial\omega_i$  do not cut through any elements in  $\mathcal{T}$  and so that the intersection of any two subdomains is either empty or a single layer of elements with thickness  $\propto h$ , see fig. 1. This decomposition naturally introduces  $n$  local meshes  $\mathcal{T}_i$  and finite element spaces  $V_i$ ,  $i = 1, \dots, n$ , where

$$V_i = \{w \in H^1(\omega_i) : w|_{\partial\Omega} = 0, w|_T \in P_1(T) \forall T \in \mathcal{T}_i\}.$$

Each local mesh is then extended by adding all the elements of  $\mathcal{T}$  which have any points below distance  $r > 0$ , i.e.

$$\mathcal{T}_i^+ = \{T \in \mathcal{T} : \inf_{x \in T, y \in \omega_i} |x - y| < r\},$$

where  $|\cdot|$  denotes the Euclidean norm. The corresponding extended subdomain is denoted by  $\omega_i^+$ . Consequently, the boundary  $\partial\omega_i^+$  will not cut through any elements and, therefore, also the extended subdomains naturally define  $n$  finite element spaces  $V_i^+$ ,  $i = 1, \dots, n$ , where

$$V_i^+ = \{w \in H^1(\omega_i^+) : w|_{\partial\Omega} = 0, w|_T \in P_1(T) \forall T \in \mathcal{T}_i^+\}.$$

As demonstrated later, the choice of the extension size  $r$  is a trade-off between the size of the reduced linear system and the size of the local problems that are solved during the basis reduction process.

A subspace of the above finite element space with Dirichlet data on the boundary  $\partial\omega_i^+ \setminus \partial\Omega$  is denoted by

$$V_{i,z}^+ = \{w \in V_i^+ : w|_{\partial\omega_i^+ \setminus \partial\Omega} = z\}.$$

In the following, we use both the space  $V_{i,z}^+$  with an arbitrary boundary condition and  $V_{i,0}^+$  with zero boundary. Moreover, we denote the trace space by

$$\partial V_i^+ = \{w \in L^2(\partial\omega_i^+) : \exists \xi \in V \text{ s.t. } \xi|_{\partial\omega_i^+} = w\}. \quad (3.1)$$

Consequently, we can define the following subproblem for each extended subdomain  $\omega_i^+$ :

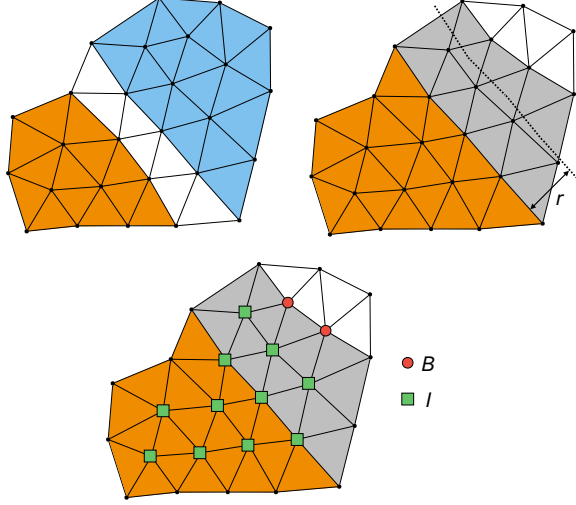


Figure 1: An example with two subdomains. (Top left.) A polygonal domain is split into overlapping subdomains  $\omega_1$  (orange and white) and  $\omega_2$  (blue and white). The subdomain  $\omega_0$  (white), consists of elements that belong to *both* subdomains – in general, to more than one subdomain. Such a decomposition can be obtained by feeding the mesh edge connectivity to a graph partitioning software, e.g., METIS [16] or Scotch [23], and finding elements that have at least one node belonging to a specific subgraph. (Top right.) The subdomain  $\omega_1$  is extended by the distance  $r$  to define  $\omega_1^+$  which then consists of the orange and the grey elements. Larger  $r$  will decrease the size of the global reduced linear system while increasing the size of the local basis reduction problem. (Bottom.) The index sets  $I$  and  $B$  are used in the definition of a discrete lifting operator from  $\partial\omega_1^+$  to  $\omega_1$  in section 4.

**Problem 3.1** (Subproblem). Given  $z \in \partial V_i^+$ , find  $u_i \in V_{i,z}^+$  such that

$$\int_{\omega_i^+} \nabla u_i \cdot \nabla v \, dx = \int_{\omega_i^+} f v \, dx \quad \forall v \in V_{i,0}^+. \quad (3.2)$$

Similarly to [1], we use problem 3.1 to construct a reduced basis within the subdomain  $\omega_i$  and, finally, combine the bases from the different subdomains in order to solve problem 2.3. The solution to problem 3.1 can be further split as  $u_i = u_{i,0} + u_{i,z}$  where  $u_{i,0}$  and  $u_{i,z}$  are solutions to the following two auxiliary problems:

**Problem 3.2** (Subproblem with zero boundary). Find  $u_{i,0} \in V_{i,0}^+$  such that

$$\int_{\omega_i^+} \nabla u_{i,0} \cdot \nabla v \, dx = \int_{\omega_i^+} f v \, dx \quad \forall v \in V_{i,0}^+. \quad (3.3)$$

**Problem 3.3** (Subproblem with zero load). Given  $z \in \partial V_i^+$ , find  $u_{i,z} \in V_{i,z}^+$  such that

$$\int_{\omega_i^+} \nabla u_{i,z} \cdot \nabla v \, dx = 0 \quad \forall v \in V_{i,0}^+. \quad (3.4)$$

Problem 3.3 defines a linear *lifting operator*  $\mathcal{Z}_i : \partial V_i^+ \rightarrow V_i, z \mapsto u_{i,z}|_{\omega_i}$ . Notice that the lifting operator restricts the solution of problem 3.3 to  $\omega_i$ . The operator coincides with the transfer operator in [6].

Let  $M_i = \dim \partial V_i^+$  and  $\{\varphi_{i,j}\}_{j=1}^{M_i}$  be a basis for  $\partial V_i^+$ . Using the solutions of problem 3.2 and problem 3.3, due to the additive splitting  $u_i = u_{i,0} + u_{i,z}$  and linearity of  $\mathcal{Z}_i$ , for each  $z = \sum_{j=1}^{M_i} b_{i,j} \varphi_{i,j} \in \partial V_i^+$  it holds

$$u_i|_{\omega_i} = u_{i,0}|_{\omega_i} + u_{i,z}|_{\omega_i} = u_{i,0}|_{\omega_i} + \mathcal{Z}_i z = u_{i,0}|_{\omega_i} + \sum_{j=1}^{M_i} b_{i,j} \mathcal{Z}_i \varphi_{i,j}.$$

This implies that the basis

$$\{u_{i,0}|_{\omega_i}, \mathcal{Z}_i \varphi_{i,1}, \dots, \mathcal{Z}_i \varphi_{i,M_i}\} \quad (3.5)$$

can represent exactly the solution of problem 3.1 for any  $z \in \partial V_i^+$ . Since the trace of the original solution to problem 2.2 belongs to  $\partial V_i^+$ , it can be also represented by the above basis.

Computing the basis (3.5) requires solving  $M_i + 1$  discrete problems in  $V_i^+$ . Unfortunately, the dimension  $M_i$  can be substantial for larger three-dimensional problems, e.g., for piecewise linear elements  $M_i$  equals to the number of nodes on the interface  $\partial \omega_i^+ \setminus \partial \Omega$ . Therefore, it is better to avoid computing and using all of the basis functions in (3.5) by performing a low-rank approximation of  $\mathcal{Z}_i$ . Fortunately, the singular values of  $\mathcal{Z}_i$  exhibits almost exponential decay and only a small subset of its range is necessary to approximate it. By performing a low-rank approximation, we arrive at the reduced basis

$$\{q_{i,0}, q_{i,1}, \dots, q_{i,m_i}\}, \quad q_{i,j} \in V_i, \quad (3.6)$$

where  $q_{i,0} = u_{i,0}|_{\omega_i}$  and  $m_i \ll M_i$ .

The details of the low-rank approximation are important for the analysis and performance of the presented technique. Hence, they shall be carefully laid out in section 4. Special care is devoted to proving how to compute the low-rank approximation in the correct norm, which is weighted with square roots of certain finite element matrices. Furthermore, a simple optimization

for computing the low-rank approximation with randomized numerical linear algebra is presented in the end of section 6.

After the reduced basis (3.6) has been computed for each subdomain  $\omega_i$ ,  $i = 1, \dots, n$ , we solve problem 2.3 within a reduced discrete space  $\tilde{V} \subset V$ ,  $\dim \tilde{V} \ll \dim V$ . The reduced space is obtained by combining the reduced bases (3.6) from different subdomains,

$$\tilde{V} = \{\sum_{i=1}^n \mathcal{S}_i w_i : w_i \in \tilde{V}_i\}, \quad \tilde{V}_i = \text{span} \{q_{i,j}\}_{j=0, \dots, m_i}, \quad (3.7)$$

where the *stitching operator*  $\mathcal{S}_i : V_i \rightarrow V$  makes any discrete functions compatible on the subdomain interfaces. This is done by setting the discrete function to zero on the boundary  $\partial\omega_i$  and further extending it by zero on the complement  $\Omega \setminus \omega_i$ .

**Definition 3.4** (Stitching operator  $\mathcal{S}_i$ ). Let  $w_i \in V_i$ . A *stitching operator*  $\mathcal{S}_i : V_i \rightarrow V$  satisfies

$$(\mathcal{S}_i w_i)(x) = \begin{cases} w_i(x) & \text{in } \omega_i \setminus \partial\omega_i, \\ 0 & \text{otherwise.} \end{cases}$$

for every node  $x$  of the mesh  $\mathcal{T}$ .

In practice, with the one node overlap of the subdomains  $\omega_i$ , the stitching operator acts as a partition-of-unity style approach in combining the subdomains. This formulation simplifies programming the method significantly as there is no explicit cut-off function to include in the finite element assembly, present in the traditional partition-of-unity method [2]. The advantage is compounded when transforming very large problems into the reduced basis, as evident in section 6. A simple one-dimensional example is presented in Figure 2.

#### 4. Low-rank approximation of $\mathcal{Z}_i$

The optimal local approximation spaces (3.6) can be computed through an eigenvalue problem [1, 7, 15] or a low-rank matrix approximation [6, 25]. We follow the latter approach, and add to the existing literature how to efficiently compute the low-rank approximation in the correctly weighted  $\ell_2$  matrix norm.

It is well known that the best  $k$ -rank approximation of a matrix in the  $\ell_2$  norm is given by its truncated singular value decomposition consisting of

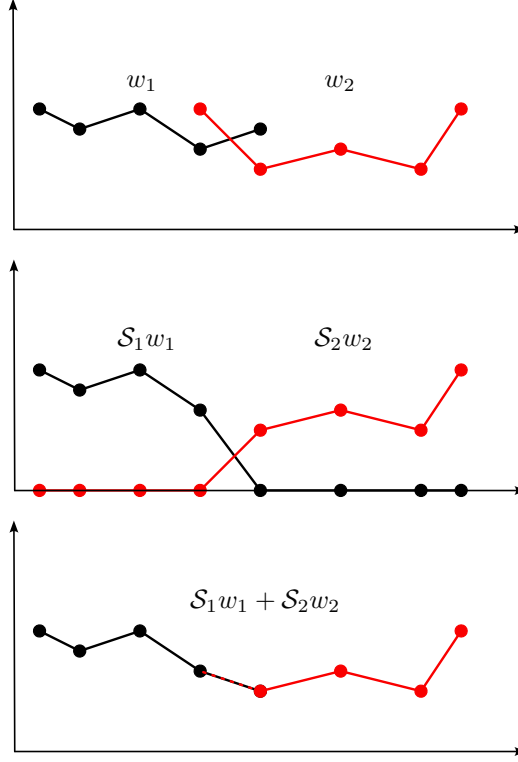


Figure 2: An example of the stitching operator with two finite element functions (red and black) over two subdomains in one dimension.

$k$  largest singular values and the corresponding singular vectors. We wish to compute a low-rank approximation of the lifting operator  $\mathcal{Z}_i$  in the natural norms of problem 3.1, i.e. the operator norm

$$\|\mathcal{Z}_i\| = \sup_{z \in \partial V_i^+} \frac{\|\mathcal{Z}_i z\|_{1, \omega_i}}{\|z\|_{\partial V_i^+}} \quad (4.1)$$

with the trace norm

$$\|z\|_{\partial V_i^+} := \inf_{\substack{v \in V_i^+, \\ v|_{\partial \omega_i^+ \setminus \partial \Omega} = z}} \|v\|_{1, \omega_i^+}.$$

The abstract fixed precision low-rank approximation problem is then of the form: given  $\epsilon > 0$ , find  $\tilde{\mathcal{Z}}_i$  such that  $\|\mathcal{Z}_i - \tilde{\mathcal{Z}}_i\| < \epsilon$  with minimal rank.

Next we explain how the low-rank approximation can be implemented in terms of  $\mathbf{Z}_i$ , the matrix representation of  $\mathcal{Z}_i$ , which is given by

$$\mathcal{Z}_i \varphi_{i,j} = \sum_k q_{i,k} (\mathbf{Z}_i \mathbf{e}_j)_k.$$

Let us denote by  $\mathbf{A}_i^+$  the stiffness matrix corresponding to problem 3.1. The stiffness matrix admits the block structure

$$\mathbf{A}_i^+ = \begin{bmatrix} \mathbf{A}_{II,i}^+ & \mathbf{A}_{IB,i}^+ \\ \mathbf{A}_{BI,i}^+ & \mathbf{A}_{BB,i}^+ \end{bmatrix}$$

where the index set  $I$  denotes the degrees-of-freedom located in the interior of  $\omega_i^+$  and  $B$  denotes the degrees-of-freedom located on the boundary  $\partial\omega_i^+ \setminus \partial\Omega$ ; see fig. 1. An alternative expression for  $\mathbf{Z}_i$ , using the stiffness matrix reads

$$\mathbf{Z}_i = \mathbf{C}_i (\mathbf{A}_{II,i}^+)^{-1} \mathbf{A}_{IB,i}^+,$$

where  $\mathbf{C}_i \in \mathbb{R}^{n_i \times N_i}$  is a restriction matrix from the interior nodes of  $V_i^+$  to  $V_i$  where  $N_i = \dim V_i^+ - M_i$ .

Now we can represent the operator norm in terms of the matrix  $\ell_2$  norm. Firstly, the numerator within the operator norm (4.1) can be written as

$$\|\mathcal{Z}_i z\|_{1,\omega_i} = \|\mathbf{R}_i \mathbf{Z}_i \boldsymbol{\beta}_z\|_{\ell_2}$$

where  $\mathbf{R}_i$  is the Cholesky factor of the finite element matrix corresponding to the bilinear form

$$\int_{\omega_i} (\nabla w \cdot \nabla v + wv) dx, \quad w, v \in V_i,$$

and  $\boldsymbol{\beta}_z = [b_1, \dots, b_{M_i}]$  is the coefficient vector corresponding to  $z \in \partial V_i^+$ .

Secondly, the denominator can be written in terms of  $\boldsymbol{\beta}_z$ , with the help of the following lemmata.

**Lemma 4.1.** *Let  $\mathbf{A}$  be a square symmetric and positive definite matrix with the block structure*

$$\mathbf{A} = \begin{bmatrix} \mathbf{A}_{II} & \mathbf{A}_{IB} \\ \mathbf{A}_{BI} & \mathbf{A}_{BB} \end{bmatrix}$$

and the Cholesky factor

$$\mathbf{R} = \begin{bmatrix} \mathbf{R}_{II} & \mathbf{R}_{IB} \\ \mathbf{0} & \mathbf{R}_{BB} \end{bmatrix}.$$

Then  $\mathbf{A}/\mathbf{A}_{II} = \mathbf{R}_{BB}^T \mathbf{R}_{BB}$  where  $\mathbf{A}/\mathbf{A}_{II} = \mathbf{A}_{BB} - \mathbf{A}_{BI} \mathbf{A}_{II}^{-1} \mathbf{A}_{IB}$  is the Schur's complement.

**Lemma 4.2.** Choose  $\mathbf{A}$  in lemma 4.1 as the finite element matrix corresponding to the bilinear form

$$\int_{\omega_i^+} (\nabla w \cdot \nabla v + wv) dx, \quad w, v \in V_i^+.$$

It holds

$$\|z\|_{\partial V_i^+} = \|\mathbf{R}_{BB,i} \boldsymbol{\beta}_z\|_{\ell_2},$$

where  $\mathbf{R}_{BB,i}$  is the bottom right Cholesky factor of  $\mathbf{A}$ .

*Proof.* See appendix Appendix A. □

Lemma 4.2 is very important in weighing the input in the matrix context. The operator norm (4.1) in the discrete setting becomes

$$\|\mathcal{Z}_i\| = \sup_{z \in \partial V_i^+} \frac{\|\mathcal{Z}_i z\|_{1, \omega_i}}{\|z\|_{\partial V_i^+}} = \max_{\boldsymbol{\beta}_z} \frac{\|\mathbf{R}_i \mathbf{Z}_i \boldsymbol{\beta}_z\|_{\ell_2}}{\|\mathbf{R}_{BB,i} \boldsymbol{\beta}_z\|_{\ell_2}} = \|\mathbf{R}_i \mathbf{Z}_i \mathbf{R}_{BB,i}^{-1}\|_{\ell_2}. \quad (4.2)$$

The equality (4.2) is crucial, but other authors have computed low-rank approximations without the weights or dismissed them due to difficulties in forming  $\mathbf{R}_{BB,i}$  and its inverse [6, Supplementary Material 4]. Without the proper weights, the low-rank matrix approximation is incompatible with the continuous problem.

We propose that Lemma 4.1 gives a novel and efficient way to compute  $\mathbf{R}_{BB,i}$  without forming the Schur complement explicitly. In particular, one computes the Cholesky factor of  $\mathbf{A}$  and reads the upper triangle matrix  $\mathbf{R}_{BB}$  from it. The inverse is not required explicitly, and  $\mathbf{R}_{BB,i}^{-1}$  arises only by solving few systems of equations, see end of section 6. Computing  $\mathbf{R}_{BB,i}$  by explicitly solving the Schur's complement  $\mathbf{A}/\mathbf{A}_{II} = \mathbf{A}_{BB} - \mathbf{A}_{BI} \mathbf{A}_{II}^{-1} \mathbf{A}_{IB}$  is much more expensive, which we exhibit in section 7. In practice, both approaches rely on the Cholesky decomposition, but the latter requires solving increasingly many large systems of equations and an additional matrix multiplication. The proper weight matrices become increasingly hard to compute without our optimization.

As a conclusion, the optimal low-rank approximation of the operator  $\mathcal{Z}_i$  in the  $H^1$  norm is obtained through the singular value decomposition of the matrix product

$$\mathbf{R}_i \mathbf{Z}_i \mathbf{R}_{BB,i}^{-1} = \mathbf{U}_i \boldsymbol{\Lambda}_i \mathbf{V}_i^T. \quad (4.3)$$

With both  $\mathbf{R}_i$  and  $\mathbf{R}_{BB,i}$  square and full rank, the low-rank matrix approximation of  $\mathcal{Z}_i$  can be given as the product  $\tilde{\mathcal{Z}}_i = \mathbf{R}_i^{-1} \mathbf{T}_i \mathbf{R}_{BB,i}$  for some  $\mathbf{T}_i$  which is obtained by truncating the singular value decomposition (4.3) in the sense that

$$\|\mathcal{Z}_i - \tilde{\mathcal{Z}}_i\| = \|\mathbf{R}_i(\mathbf{Z}_i - \tilde{\mathbf{Z}}_i)\mathbf{R}_{BB,i}^{-1}\|_{\ell_2} = \|\mathbf{R}_i \mathbf{Z}_i \mathbf{R}_{BB,i}^{-1} - \mathbf{T}_i\|_{\ell_2} < \epsilon, \quad (4.4)$$

where  $\epsilon > 0$  is a user specified tolerance. Moreover, the reduced basis  $q_{1,i}, \dots, q_{m_i,i}$  in (3.6) is given by the columns of  $\mathbf{R}_i^{-1} \mathbf{U}_i$  which are directly computable, see section 6. The number of columns  $m_i \ll M_i$  is indirectly specified by the extension parameter  $r$  and the tolerance  $\epsilon$ .

## 5. Error analysis

Next, we derive the error estimate for the reduced discrete problem, problem 2.3. The analysis is similar to [1, 6]. The local basis reduction error can be controlled solely with the tolerance parameter,  $\epsilon > 0$ , which can be adjusted so that the global error is dominated by the finite element discretization error. In the following  $\tilde{V}$  and  $\tilde{V}_i$ ,  $i = 1, \dots, n$ , are given by (3.7).

Let  $\phi \in H_0^1(\Omega)$  be the continuous solution to problem 2.1 and  $u \in V$  be the discrete solution to problem 2.2. Further, let  $\tilde{u} \in \tilde{V}$  be the reduced solution to problem 2.3. Because (2.4) is a Ritz–Galerkin method, there exists  $C > 0$  so that

$$\|\phi - \tilde{u}\|_{1,\Omega} \leq C \|\phi - \tilde{v}\|_{1,\Omega} \leq C(\|\phi - u\|_{1,\Omega} + \|u - \tilde{v}\|_{1,\Omega}) \quad \forall \tilde{v} \in \tilde{V}. \quad (5.1)$$

The first term can be estimated using techniques from the standard finite element method a priori error analysis. Thus, we focus on the second term  $\|u - \tilde{v}\|_{1,\Omega}$  and demonstrate how  $\tilde{v}$  can be constructed subdomain-by-subdomain to reveal its dependency on the tolerance  $\epsilon > 0$  of the low-rank approximation.

### 5.1. Estimate on a single subdomain

For the solution  $u$  of problem 2.2 it holds  $u|_{\omega_i} = u_{i,0}|_{\omega_i} + \mathcal{Z}_i(u|_{\partial\omega_i^+})$  where  $u_{i,0}$  is the solution of problem 3.2. Let

$$\tilde{v}_i = u_{i,0}|_{\omega_i} + \tilde{\mathcal{Z}}_i(u|_{\partial\omega_i^+}) \quad (5.2)$$

where  $\tilde{\mathcal{Z}}_i : \partial V_i^+ \rightarrow \tilde{V}_i$  is defined through the action of the low-rank matrix approximation  $\tilde{\mathcal{Z}}_i$ . Notice that the nontrivial load term  $u_{i,0}$  is identical for both  $u$  and  $\tilde{v}_i$ . Therefore, the error can be bounded as

$$\|u - \tilde{v}_i\|_{1,\omega_i} \leq \|\mathcal{Z}_i - \tilde{\mathcal{Z}}_i\| \|u|_{\partial\omega_i^+}\|_{\partial V_i^+} \leq \|\mathcal{Z}_i - \tilde{\mathcal{Z}}_i\| \|u\|_{1,\omega_i^+}. \quad (5.3)$$

Combining (5.3) with (4.4), we arrive to the following lemma.

**Lemma 5.1.** *Let  $u \in V$  be the solution of problem 2.2 and  $\tilde{v}_i \in \tilde{V}_i \subset V_i$  be defined via (5.2). It holds*

$$\frac{\|u - \tilde{v}_i\|_{1,\omega_i}}{\|u\|_{1,\omega_i^+}} < \epsilon.$$

Thus, we interpret the truncation tolerance  $\epsilon$  as a local bound for the relative error caused by the introduction of the reduced basis. The bound is in almost all practical cases very crude. This is because the first inequality in (5.3) moves from a specific boundary trace of  $u$  and  $\tilde{v}_i$  to the operator norm  $\|\mathcal{Z}_i - \tilde{\mathcal{Z}}_i\|$ , which has to account for *all possible boundary conditions*, including very pathological ones. This means that the method tends to be locally considerably more accurate than the given tolerance  $\epsilon$ , especially when a relatively smooth load  $f$  is used.

## 5.2. Full error estimate

Any discrete function  $v \in V$  can be split as

$$v = \sum_{i=1}^n \mathcal{S}_i(v|_{\omega_i}),$$

where the stitching operator  $\mathcal{S}_i$  is given by definition 3.4. Moreover, all functions in the reduced space  $\tilde{V}$  have the above form by definition. Hence, we will first show an asymptotic bound for the action of  $\mathcal{S}_i$  and then present the full error estimate which combines the result of lemma 5.1 from all subdomains.

**Lemma 5.2.** *There exists  $C > 0$  such that*

$$\|\mathcal{S}_i\| \leq C(1 + h^{-1}).$$

*Proof.* The operator norm is

$$\|\mathcal{S}_i\| = \sup_{w \in V_i} \frac{\|\mathcal{S}_i w\|_{1,\Omega}}{\|w\|_{1,\omega_i}}.$$

We start by bounding the numerator. There exists  $C_{inv} > 0$ , independent of  $h$  [27], such that

$$\|\mathcal{S}_i w\|_{1,\Omega}^2 = \|\mathcal{S}_i w\|_{0,\Omega}^2 + \|\nabla \mathcal{S}_i w\|_{0,\Omega}^2 \leq (1 + C_{inv} h^{-2}) \|\mathcal{S}_i w\|_{0,\Omega}^2. \quad (5.4)$$

Notice that  $\text{supp}(\mathcal{S}_i w) \subset \omega_i$  so  $\|\mathcal{S}_i w\|_{0,\Omega} \leq \|w\|_{0,\omega_i}$ .

Now, the denominator is bounded below by

$$\|w\|_{0,\omega_i}^2 \leq \|w\|_{0,\omega_i}^2 + \|\nabla w\|_{0,\omega_i}^2 = \|w\|_{1,\omega_i}^2,$$

thus

$$\|\mathcal{S}_i\| \leq \frac{\sqrt{1 + C_{inv} h^{-2}} \|w\|_{0,\omega_i}}{\|w\|_{0,\omega_i}} \leq C(1 + h^{-1}).$$

□

**Remark 1.** The  $h^{-1}$  dependency fortunately manifests only in few pathological cases, and even in those mostly locally. This dependency could be circumvented, e.g., by using the Lagrange multiplier method or Nitsche's method for combining the local solutions. However, it will be present via the derivative of the cut-off function also when using the standard partition of unity approach.

**Criterion 5.3** (Partition overlap). *Let the triangulation/tetrahedralization  $\mathcal{T}$  be partitioned to  $n$  overlapping local meshes  $\mathcal{T}_i^+$ . Let  $m \in \mathbb{N}, m < n$ , such that any element  $T \in \mathcal{T}$  is included in at most  $m$  local meshes.*

Criterion 5.3 is satisfied when the extension parameter  $r$  is kept within reasonable limits, such as under half of the subdomain diameter. Then,  $m$  will be a very small integer as any elements are included only in the intersection of the nearest few subdomains. The number of subdomains  $n$  can, however, grow without influencing  $m$ . Hence, for relevant problems and decompositions  $m \ll n$ .

We can use criterion 5.3 to connect the bound (5.3) more effectively with a global error bound. The issue with (5.3) is that the norm is transformed from  $V_i$  to  $V_i^+$ . Given criterion 5.3, it is immediate that

$$\sum_{i=1}^n \|u\|_{1,\omega_i^+} \leq m \|u\|_{1,\Omega}.$$

This is also a loose bound because most elements only belong to individual subdomains. We are now ready to present the global error estimate.

**Theorem 5.4.** *Let the finite element mesh partition satisfy criterion 5.3. Then there exists  $C > 0$  such that*

$$\|\phi - \tilde{u}\|_{1,\Omega} \leq C(\|\phi - u\|_{1,\Omega} + m(1 + h^{-1})\epsilon \|u\|_{1,\Omega}). \quad (5.5)$$

*Proof.* As in (5.1), the error can be split into standard finite element error and the reduction error

$$\|\phi - \tilde{u}\|_{1,\Omega} \leq C\|\phi - \tilde{v}\|_{1,\Omega} \leq C(\|\phi - u\|_{1,\Omega} + \|u - \tilde{v}\|_{1,\Omega}) \quad \forall \tilde{v} \in \tilde{V}. \quad (5.6)$$

Note that the standard finite element error is proportional to  $h\|f\|_{0,\Omega}$  [5].

The finite element solution  $u$  can be written as

$$u = \sum_{i=1}^n \mathcal{S}_i(u|_{\omega_i}).$$

Therefore, choosing  $\tilde{v} \in \tilde{V}$  in the best approximation result (5.6) as

$$\tilde{v} = \sum_{i=1}^n \mathcal{S}_i(\tilde{v}_i),$$

where  $\tilde{v}_i$  is given by the expression (5.2), leads to

$$\begin{aligned} \|u - \tilde{v}\|_{1,\Omega} &\leq \sum_{i=1}^n \|\mathcal{S}_i\| \|u|_{\omega_i} - \tilde{v}_i\|_{1,\omega_i} \\ &\leq \sum_{i=1}^n C(1 + h^{-1}) \|u - \tilde{v}_i\|_{1,\omega_i} \\ &\leq \sum_{i=1}^n C(1 + h^{-1}) \epsilon \|u\|_{1,\omega_i^+} \\ &\leq C(1 + h^{-1}) \epsilon m \|u\|_{1,\Omega}. \end{aligned} \quad (5.7)$$

Combining the above with (5.6) concludes the proof.  $\square$

Theorem 5.4 provides a global error bound for our method. The error is a combination of the conventional finite element error and the error introduced by the projection onto a smaller solution space which is proportional to the parameter  $\epsilon$ . Further, the more challenging  $h^{-1}$  dependency is due to our stitching operator  $\mathcal{S}_i$  that luckily manifests only in few pathological cases, and even in those mostly locally. This dependency could be circumvented, e.g., by using the Lagrange multiplier method or Nitsche’s method for combining the local solutions, but it will be present via the derivative of the cut-off function also when using the standard partition of unity approach. In practice, the reduction error is negligible even for very relaxed parameterization, primarily due to the pessimistic bound (5.3). The method can be easily tuned such that the finite element error is the limiting term, see the numerical results in section 7.

## 6. Parallel implementation

In this section, we propose an outline to implement our methodology in a setting with one master node and a host of worker nodes. Given a mesh  $\mathcal{T}$ , number of subdomains  $n$ , tolerance  $\epsilon$ , and optionally a rule to define the subdomain extension parameter  $r$ , the program outputs a solution to problem 2.3 with smaller than  $\epsilon$  local relative error compared to problem 2.1 as per lemma 5.1. The full error to the theoretical solution of problem 2.1 is bounded by theorem 5.4.

The computational framework follows a three-step structure:

- (1) preprocessing the data into extended submeshes;
- (2) computing the optimal local bases; and
- (3) transforming the global system and solving the smaller problem.

Steps (1) and (3) can be computed on the master node while step (2) can be completely parallelized in a distributed setting without node communication; see fig. 3. For testing purposes, step (2) may be run sequentially on a single computer. Code corresponding to the framework using `scikit-fem` [13] can be found from [17]. This section omits some optimizations included in the code for clarity. In section 7, the scaling tests suggest approximate hardware requirements for problems of different sizes. We will now address steps (1)-(3) in order, but focus primarily on step (3) because the first two are direct applications of section 3 and 4.

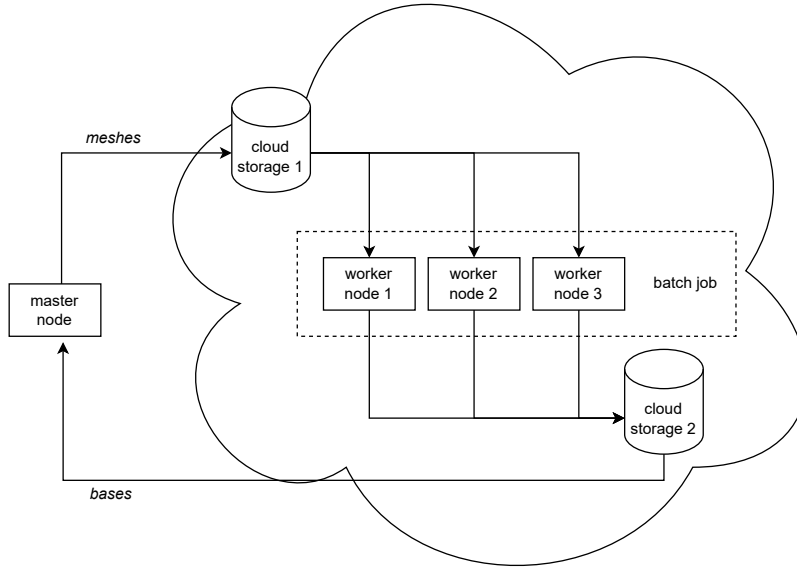


Figure 3: A high level overview of the data flow in our distributed implementation of step (2). Decomposing the mesh into overlapping subdomains is done by the master node in step (1). The overlapping meshes are then uploaded to a cloud storage bucket where the worker nodes are able to access the files. The worker nodes are virtual machines launched as a batch job. The figure depicts an example with three worker nodes/subdomains. The worker nodes write their output data to a separate cloud storage bucket which can be accessed by the master node in order to proceed with step (3).

### *Step (1)*

Beginning with preprocessing, the connectivity between the mesh nodes is interpreted as a graph and the nodes are split into  $n$  overlapping subdomains using a graph partitioning algorithm [16, 23] according to fig. 1. The submeshes  $\mathcal{T}_i^+$ , which include information of both the subdomains  $\omega_i$  and the extended subdomains  $\omega_i^+$ , and their neighboring relations are saved to files. This concludes step (1).

### *Step (2)*

The files are sent to worker nodes for computing the reduced local bases. Before going into computations, it is worth to describe briefly how the local bases are used to transform the system in the end. Let  $\mathbf{Q}_i$  denote the reduced local basis corresponding to  $\omega_i$  and  $\mathbf{A}$  the global stiffness matrix

corresponding to eq. (2.3). In step (3), we would like to project the original system for

$$\begin{aligned} \mathbf{Q}^T \mathbf{A} \mathbf{Q} &= \begin{pmatrix} \mathbf{Q}_1 & & \mathbf{0} \\ & \ddots & \\ \mathbf{0} & & \mathbf{Q}_n \end{pmatrix}^T \begin{pmatrix} \mathbf{A}_{11} & \cdots & \mathbf{A}_{1n} \\ \vdots & \ddots & \vdots \\ \mathbf{A}_{n1} & \cdots & \mathbf{A}_{nn} \end{pmatrix} \begin{pmatrix} \mathbf{Q}_1 & & \mathbf{0} \\ & \ddots & \\ \mathbf{0} & & \mathbf{Q}_n \end{pmatrix} \\ &= \begin{pmatrix} \mathbf{Q}_1^T \mathbf{A}_{11} \mathbf{Q}_1 & \cdots & \mathbf{Q}_1^T \mathbf{A}_{1n} \mathbf{Q}_n \\ \vdots & \ddots & \vdots \\ \mathbf{Q}_n^T \mathbf{A}_{n1} \mathbf{Q}_1 & \cdots & \mathbf{Q}_n^T \mathbf{A}_{nn} \mathbf{Q}_n \end{pmatrix}. \end{aligned} \quad (6.1)$$

Hence, in step (2), we compute  $\mathbf{Q}_i$  and the product  $\mathbf{Q}_i^T \mathbf{A}_{ii} \mathbf{Q}_i$  and send those to the master node.

We proceed first by assembling a local system from the local mesh corresponding to  $\omega_i^+$ . Then, creating the optimal reduced basis for  $\omega_i$  proceeds again in two substeps. Firstly, problem 3.2 is solved and restricted to  $\omega_i$  to obtain the first basis function. Secondly, the rest of the basis is obtained by computing the matrix-version of the lifting operator  $\mathcal{Z}_i$  as

$$\mathbf{Z}_i = \mathbf{C}_i (\mathbf{A}_{II,i}^+)^{-1} \mathbf{A}_{IB,i}^+.$$

Next, the weight matrices  $\mathbf{R}_i$  and  $\mathbf{R}_{B,i}^+$  are solved following section 4, and the low-rank approximation computed per (4.4). The left singular vectors of the low-rank approximation can be denoted  $\mathbf{U}_{i,\epsilon}$ . Then, the energy norm weights are removed and the range restricted,  $\mathbf{Q}_i = \mathbf{D}_i \mathbf{R}_i^{-1} \mathbf{U}_{i,\epsilon}$ , where  $\mathbf{D}_i$  is another restriction matrix from the degrees-of-freedom corresponding to  $\omega_i$  to the degrees-of-freedom corresponding to the interior of  $\omega_i$ . The restriction matrix  $\mathbf{D}_i$  acts as the stitching operator in definition 3.4. The range now corresponds to the correct solution space. To improve accuracy and to reduce memory usage and transfer, a generalized eigenvalue problem is still solved for a slightly updated basis. This optimization diagonalizes the diagonal blocks of (6.1). The details can be inferred from our source code [17].

Step (2) is finished by sending the relevant information back to the master node. This includes the bases  $\mathbf{Q}_i$ , the projected local problems and some indexing information of  $\omega_i$  and  $\partial\omega_i^+$ . This data is sufficient for transforming the global system.

### *Step (3)*

The challenge in step (3) is in the transformation (6.1) for extremely large  $\dim V$ . While the global stiffness matrix  $\mathbf{A}$  is very sparse, the number

of degrees-of-freedom makes direct computation of  $\mathbf{Q}^T \mathbf{A} \mathbf{Q}$  infeasible. Fortunately, the matrix product (6.1) can be constructed implicitly, assembling neither  $\mathbf{A}$  nor  $\mathbf{Q}$ . In particular, the diagonal submatrices were already computed in step (2). Further, the vast majority of the off-diagonal submatrices  $\mathbf{Q}_i^T \mathbf{A}_{ij} \mathbf{Q}_j$ , which correspond to the nodes in the interiors of  $\omega_i$  and  $\omega_j$ ,  $i \neq j$ , are predictably zero.

The nonzero off-diagonals can be constructed as follows. Let the set of elements that are included in at least two subdomains be denoted by  $\omega_0 = \cup_{i=1}^n \cup_{j=1}^n (\omega_i \cap \omega_j)$ . The nonzero values correspond to the interior degrees-of-freedom of  $\omega_i$  and  $\omega_j$  that influence the same interfacing element in  $\omega_0$ , and these values are dependent on *the interfacing elements only*. Note that each subdomain is neighboring only a minority of the other subdomains. For non-neighboring subdomains, the matrix  $\mathbf{Q}_i^T \mathbf{A}_{ij} \mathbf{Q}_j$  is zero as  $\mathbf{A}_{ij}$  is a zero matrix. For neighboring subdomains, the intersection  $\omega_i \cap \omega_j$  is still very small, which means that  $\mathbf{A}_{ij}$  is very sparse. Moreover, the nonzero values are known in advance to correspond to the degrees-of-freedom which are included in  $(\omega_i \cap \omega_j) \setminus \partial\Omega$ .

Hence, the off-diagonal submatrices can be also computed in parallel with respect to a stiffness matrix  $\mathbf{A}_0$  assembled over the set of interfacing elements  $\omega_0$  and indexed on the respective boundary degrees-of-freedom. This is a much cheaper procedure:  $\mathbf{A}_0$  is *extremely* sparse and hence fits into memory easily even for extremely large problems. Moreover, it becomes evident that we do not need the full  $\mathbf{Q}_i$  from step (2) but only the matrix rows corresponding to the boundary degrees-of-freedom. The off-diagonal products are then with respect to a small subset of the degrees-of-freedom and almost all of the products are predictably zero due to the existence of non-neighboring subdomains.

Projecting the stiffness matrix onto the optimal basis can be now done in parts, by iterating over the pairs of neighboring subdomains in parallel. The projection of the system is then possible to compute on a laptop even for large problems. Without this optimization, scaling the method requires prohibitive amounts of memory. The projection of the right-hand side was already done in step (2). The reduced global system is then fast to solve using an iterative method such as the preconditioned conjugate gradient method and a diagonal preconditioner.

*Randomized numerical linear algebra*

The whole procedure can be managed on a laptop master node for considerable problem sizes if the bulk of the work is distributed to worker nodes in step (2). Still, constructing  $\mathbf{Z}_i$  and its low-rank approximation scale poorly in step (2). Luckily, both can be optimized as follows.

The tool we use is *sketching* from randomized numerical linear algebra [21]. In a nutshell, the [14, Algorithm 4.1] samples a smaller standard Gaussian random matrix  $\mathbf{S}_i \in \mathbb{R}^{M_i \times k_i}$ ,  $k_i < M_i$ , mapping it with the weighted  $\mathbf{Z}_i$ , and performing a  $\mathbf{QR}$  factorization on the smaller matrix product

$$\hat{\mathbf{Q}}_i \hat{\mathbf{R}}_i = \mathbf{R}_i \mathbf{C}_i \mathbf{A}_{II,i}^{-1} \mathbf{A}_{IB,i} \mathbf{R}_{BB,i}^{-1} \mathbf{S}_i.$$

The resulting  $\hat{\mathbf{Q}}_i$  spans a subspace of the image of the weighted  $\mathbf{Z}_i$  determined by random boundary conditions. This is similar to [6], but we have added the required inner product matrices  $\mathbf{R}_i$  and  $\mathbf{R}_{BB,i}^{-1}$ . The expected and tail errors from using this approach are detailed in appendix Appendix B and we discuss how to choose the sketching parameter at the end of section 7.1.

However, compared to doing the SVD of the weighted  $\mathbf{Z}_i$  directly to find the smallest local approximation space for  $\epsilon$ , the local spaces from sketching can be much larger than desired due to oversampling. We noticed that even iterative sketching procedures often generated local approximation spaces twice the size of an explicit SVD. The optimal local space is a subspace of  $\hat{\mathbf{Q}}_i$  with a very high probability, so the SVD could be done the for sketched matrix. However, this produces poor results due to scaling singular values with the random boundary conditions.

We propose an efficient approach to find the optimal local approximation space by projecting the image of  $\mathbf{Z}_i$  onto  $\hat{\mathbf{Q}}_i$ , and then doing an SVD for the matrix product

$$\hat{\mathbf{Q}}_i^T \mathbf{R}_i \mathbf{C}_i \mathbf{A}_{II,i}^{-1} \mathbf{A}_{IB,i} \mathbf{R}_{BB,i}^{-1}. \quad (6.2)$$

Taking the singular vectors that correspond to singular values greater than tolerance for  $\hat{\mathbf{U}}_{i,\epsilon}$ , the updated basis is given by  $\mathbf{Q}_i = \mathbf{D}_i \mathbf{R}_i^{-1} \hat{\mathbf{Q}}_i \hat{\mathbf{U}}_{i,\epsilon}$ . This is known as the randomized SVD [21]. The problem is that computing (6.2) from right-to-left now requires solving  $M_i$  large systems of equations in  $\mathbf{A}_{II,i}^{-1} \mathbf{A}_{IB,i}$  compared to  $k_i$  in sketching. We resolve this issue by noting that by transposing the matrix product (6.2) twice, it can be computed with two left solves as

$$\hat{\mathbf{Q}}_i^T \mathbf{R}_i \mathbf{C}_i \mathbf{A}_{II,i}^{-1} \mathbf{A}_{IB,i} \mathbf{R}_{BB,i}^{-1} = (\mathbf{R}_{BB,i}^{-T} ((\mathbf{A}_{II,i}^{-T} (\hat{\mathbf{Q}}_i^T \mathbf{R}_i \mathbf{C}_i)^T)^T \mathbf{A}_{IB,i})^T)^T,$$

so that the linear solves are with respect to  $k_i$  instead of  $M_i$  right-hand sides. This retains the asymptotics of plain sketching and approximately only doubles the hidden coefficient.

Our approach produces *practically the same optimal bases as explicitly constructing weighted  $\mathbf{Z}_i$  and doing an SVD, with a very high probability*, while being a magnitude faster than the explicit variant for relevant problem sizes. In contrast, creating the reduced basis by sketching only introduces plenty of redundant dimensions to the projection. Achieving the smallest reduced bases is important for very large problems to fit the reduced global problem into memory. Our optimization enjoys the benefits of both speed and small dimensionality.

Further, we repeat that the bound in lemma 5.1 is very crude, and hence the local error tends to be much smaller than the tolerance  $\epsilon$ . This is numerically supported in section 7.1. As a result, we experienced the explicit and randomized variants in step (2) to produce practically identical global errors in our simulations.

## 7. Numerical experiments

We provide three kinds of numerical results to support the theoretical discussion. First, we introduce scaling tests on a unit cube with evenly spaced tetrahedral elements and the canonical hat basis, with the model order reduction implemented in a cloud environment. The numerical error and the use of computational resources are analyzed in detail. Secondly, we solve an example of (2.1) with a nonconstant parameter  $a = a(x)$ . Thirdly, we showcase the methodology in the case of a "2.5-dimensional" engineering geometry, which provides a more realistic application with low-dimensional partition interfaces.

### 7.1. Scaling tests

Cube is one of the most challenging objects geometrically for the method as decomposing it into subdomains produces large interfaces and hence larger optimal reduced bases. The scaling test included 7 cases of increasing size up to 86 350 888 degrees-of-freedom. Problem 2.1 with load

$$f = 2\sqrt{900}((1-x)x(1-y)y + (1-x)x(1-z)z + (1-y)y(1-z)z)$$

on  $\Omega = [0, 1]^3$  was approximated by solving problem 2.2 using the domain decomposition method. Such a loading was chosen because the energy norm

of the corresponding analytical solution  $\phi$  is equal to 1. Then by the Galerkin orthogonality, the error can be computed as

$$\|\nabla(\phi - \tilde{u})\|_{0,\Omega} = (\|\nabla\phi\|_{0,\Omega}^2 - \|\nabla\tilde{u}\|_{0,\Omega}^2)^{1/2} = (1 - \mathbf{x}^T \mathbf{Q}^T \mathbf{A} \mathbf{Q} \mathbf{x})^{1/2},$$

where  $\mathbf{x}$  is the reduced solution vector.

The tolerance was set to  $\epsilon = 1\text{e-}2$  which now corresponds to the maximum relative error of 1% for each subdomain. This is enough even for the largest cases, evident in table 2 and fig. 4, due to the looseness of the bound in lemma 5.1. The number of subdomains was chosen such that the number of degrees-of-freedom on each subdomain would be in few thousands. The mesh partitions were produced by METIS [16] up to case 8 and with a custom regular cube partitioning algorithm afterwards; the bottleneck on the master node was ultimately the memory usage of the mesh preprocessing. The extension parameter  $r$  was defined via mesh node hops, hereon called  $r$ -hops, including into the extension all nodes within  $r$  edges from the subdomain. The hops were specified to approximately double the diameter of the subdomains. In a three-dimensional setting, this roughly eightfolds the subdomain volume or the number of degrees-of-freedom in a computational setting.

The local reduced bases were computed in Google Cloud using the last sketching procedure detailed at the end of section 6 with  $k_i = \lfloor M_i/8 \rfloor$ . This choice is justified by the spectra of the local operators, discussed at appendix Appendix C. The cloud worker nodes were employed with `c2-standard-4` machine type and `debian-11-bullseye-v20230411` image at spot prices for lower costs. Up to case 8,  $n/5$  virtual machines were reserved so that each instance computed five local problems. From case 9 and onwards 1000 instances were reserved. Solving a local problem took in general under a minute of wall clock time, but due to waiting for resources at spot prices the mean times could increase to three minutes per problem across the largest jobs.

Table 1: Computational environment for the scaling tests.

Node	OS	CPU	Threads	RAM
Master	Ubuntu 22.04 LTS	Intel Core i5-1335U	12	32GB
Worker	Debian Bookworm 12.5	Intel Xeon Gold 6254	4	4GB

The local reduced bases were transferred back to the master node, where the global stiffness matrix was transformed using optimizations introduced in

section 6. The reduced linear system of equations was finally solved using the conjugate gradient method with a diagonal preconditioner. Even for case 11, the postprocessing and the solve took roughly four hours, where the computational time concentrated almost exclusively on the system transformation. The master and worker node specifications are detailed in table 1.

The results can be found from table 2 and fig. 4. The error from the theoretical solution decreases with  $h$  as expected. The reduction error, i.e. the error between the conventional FE solution and our domain decomposition method, stays relatively constant at double the local error bound. The Google Cloud cost in dollars is mainly from computational resources with some additional costs from data transfer and storage.

Table 2: Scaling tests with  $\epsilon = 1e-2$ . The reduction error has not been computed for cases 8 and above due to the large sizes of the original systems.

Case	dim( $V$ )	$n$	$r$ -hop	$h$	error	red. error	cost
4	4 233	6	4	1.5e-1	1.6e-1	9.0e-5	≤\$0.1
5	30 481	30	5	9.9e-2	8.0e-2	2.1e-4	≤\$0.1
6	230 945	100	6	4.9e-2	4.1e-2	2.6e-4	\$0.16
7	1 000 000	400	6	1.7e-2	2.1e-2	2.0e-4	\$0.73
8	10 648 000	4 000	6	7.9e-3	9.5e-3	-	\$4.36
9	21 952 000	8 000	6	6.2e-3	7.5e-3	-	\$8.64
10	42 875 000	15 625	6	4.9e-3	6.0e-3	-	\$15.75
11	86 350 888	39 304	6	3.9e-3	4.7e-3	-	\$39.85

Figure 5 displays the reduced solution and its error compared to the FE solution for case 7. The approximation is practically exact inside the subdomains, but some error persists on the subdomain interfaces.

Table 3 presents how the global system size and conditioning is improved for cases in table 2, although with small increase in the number of nonzero values. The reductions are significant with the reduced bases having around 20–30 times fewer degrees-of-freedom than the original bases. The condition numbers are also about half of the original system value. Unfortunately, the relative fill-ins of the reduced stiffness matrices are much larger because the support of the reduced bases are larger than the support of the original piecewise linear finite element bases, and the nonzero off-diagonal submatrices are dense. The size of the dense blocks can be reduced by further increasing the

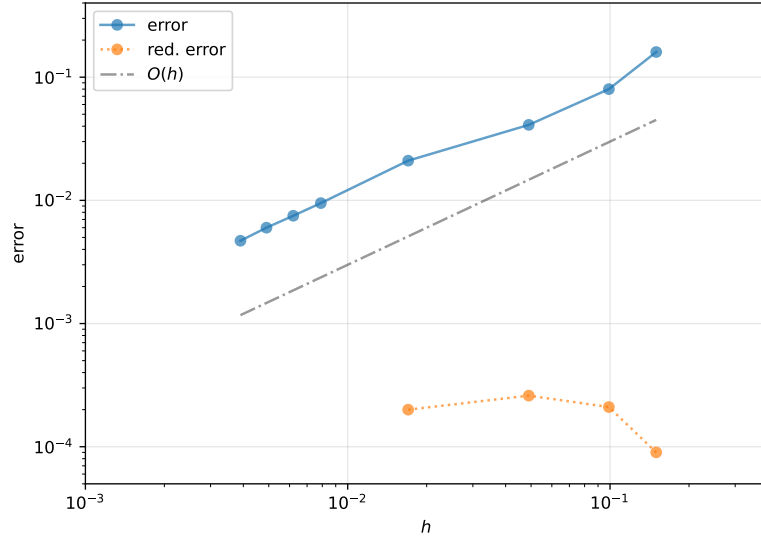


Figure 4: Convergence of the method on a log-log scale. The  $x$ -axis depicts the mesh parameter  $h$ , and the  $y$ -axis shows the errors  $\|\nabla(\phi - \tilde{u})\|_{0,\Omega}$ , the reduction errors  $\|\nabla(u - \tilde{u})\|_{0,\Omega}$  and the theoretical FEM convergence rate. The reduced method follows the conventional rate since the reduction error stays well below the FEM error. The reduction errors were not computed for the largest cases due to limitations in scaling the conventional FEM.

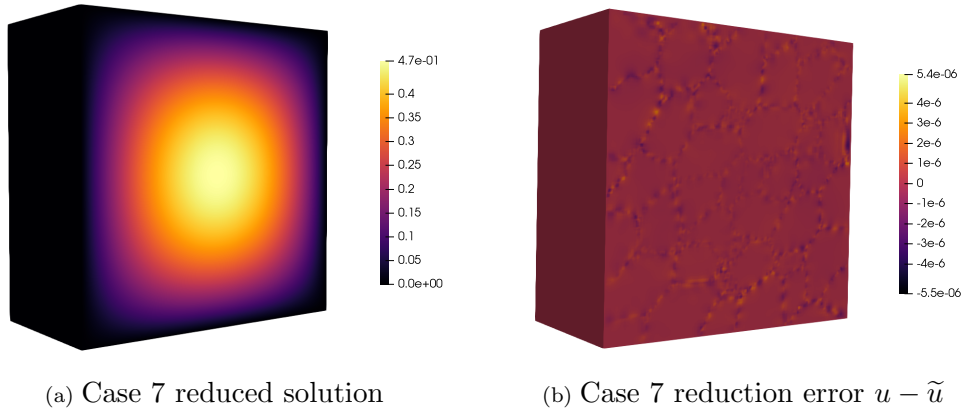


Figure 5: Case 7 reduced solution and error. The error is negligible and concentrates on the subdomain interfaces.

number of extension hops. However, this cost is negligible compared to the fact that it is infeasible to assemble the original stiffness matrix altogether with the same memory.

Table 3: Dimensions, number of nonzeros and condition numbers of the original and reduced stiffness matrices for the scaling tests in table 2. The cases 8 and below used METIS in the graph partitioning. The cases 9 and above used a custom block partitioning algorithm which splits the cube into smaller cubes of equal size. The regular shape of the cubical subdomains and their extensions explains the drop in the number of nonzeros from case 8 to case 9. The number of nonzeros and the condition numbers have not been computed for the cases 8 and above due to the high computational efforts involved.

Case	$\dim(V)$	$\dim(\tilde{V})$	$\text{nnz}(\mathbf{A})$	$\text{nnz}(\tilde{\mathbf{A}})$	$\kappa(\mathbf{A})$	$\kappa(\tilde{\mathbf{A}})$
4	4 233	178	56 195	21 888	34	50
5	30 481	1 436	424 627	682 710	445	211
6	230 945	6 880	3 289 443	5 800 292	2161	816
7	1 000 000	35 041	6 940 000	42 801 805	3971	2272
8	10 648 000	425 194	-	659 025 526	-	-
9	21 952 000	895 208	-	600 208 952	-	-
10	42 875 000	1 782 383	-	1 219 492 727	-	-
11	86 350 888	4 019 216	-	2 466 745 712	-	-

### 7.2. Subproblem scaling

We claimed that the method is difficult to scale without optimizing the computation of  $\mathbf{R}_{BB,i}$ , the construction of the optimal reduced basis  $\mathbf{Q}_i$  and the projection of the system to the reduced basis  $\mathbf{Q}^T \mathbf{A} \mathbf{Q}$ . Our optimization for the first problem was given in section 4 while optimizations for the latter two were delineated in section 6. We now present numerical evidence of the subproblem scaling focusing first on the two subproblems that are local and then examining the global transformation of the system to the reduced basis. All computations were completed on the master node in table 1.

Figure 6 compares the scaling of  $\mathbf{R}_{BB,i}$  and  $\mathbf{Q}_i$  by first computing the desired subproblems with a straightforward approach and secondly with our optimizations. For  $\mathbf{R}_{BB,i}$ , explicitly computing the Schur complement tends to scale quadratically in wall clock time compared to sub-quadratic scaling of the Cholesky decomposition for the extended local problem. The effect becomes more pronounced when we compute the smallest possible basis  $\mathbf{Q}_i$  given a tolerance  $\epsilon = 1e-2$ . Using a full SVD after explicitly constructing

weighted  $\mathbf{Z}_i$  scales superquadratically, while our optimized version of the randomized SVD retains the same sub-quadratic scaling as computing the  $\mathbf{R}_{BB,i}$ . Importantly, the reduction error is still kept well below FEM error while the dimensionality of  $\mathbf{Q}_i$  remains consistently within approximately 5% of the direct SVD. Already for medium-sized problems our optimizations are a magnitude faster while requiring roughly half the memory of straightforward approaches. The performance gap increases with problem size in both cases, and will effect the requirements and costs of worker nodes in table 1.

Next, fig. 7 presents how our projection approach improves upon the direct projection by full matrix multiplications  $\mathbf{Q}^T \mathbf{A} \mathbf{Q}$ . Both approaches rely on sparse matrix multiplication with the same number of nonzeros, but the difference is that the explicit method constructs both  $\mathbf{Q}$  and  $\mathbf{A}$ , while our optimized version constructs neither explicitly and multiplies only nonzero indices. Expectedly, the approaches have the same asymptotics, but our optimized version has a magnitude faster computational times. Crucially, the direct approach runs out of memory using the master node in table 1 already when degrees-of-freedom are in the single millions, while the optimized approach can project systems closer to 100 million degrees-of-freedom. Without optimizing the projection to the reduced basis, scaling the method is indeed impossible in memory-constrained environments.

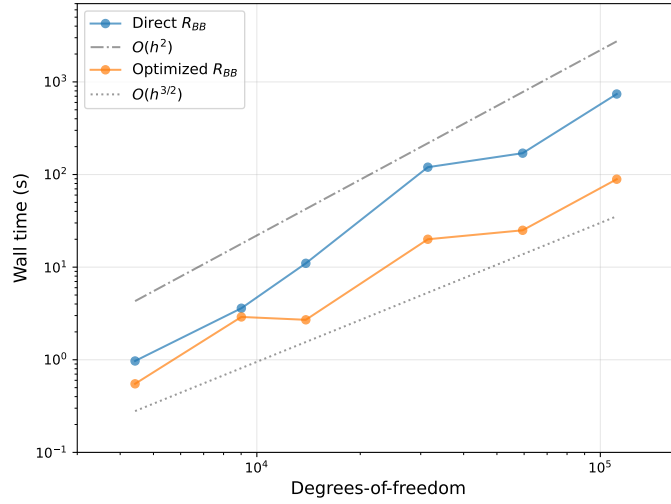
### 7.3. Nonconstant $a$

The error analysis in section 5 is done under the assumption that the material parameter in the governing equation (2.1) is  $a = 1$ . Thus, the analysis does not answer to, e.g., how the different constants depend on a spatially varying  $a = a(x)$  and whether the algorithm should be changed to accommodate this. We will now present preliminary numerical results using a space-dependent material field,

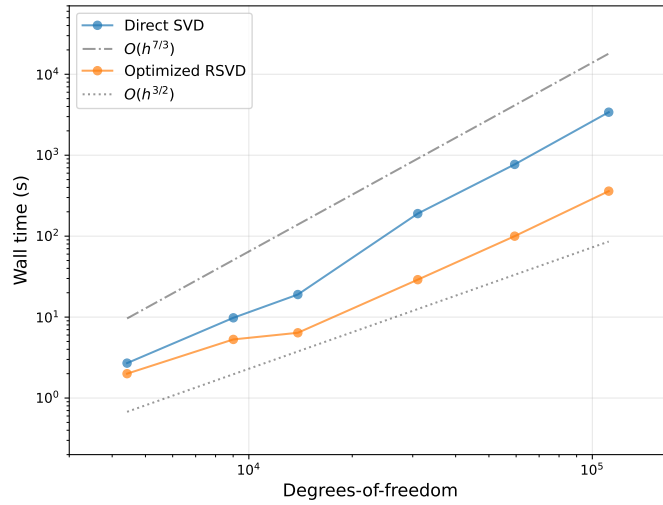
$$a = a(x) = 10^k \sin(100x) + 10^k + 1, \quad k = 1, 2, 3,$$

and leave more detailed error analysis for future work. In the case of  $k = 3$ , the ratio between the largest and the smallest values of  $a(x)$  is 2001 : 1.

The finite element mesh of case 5 in table 2 is suitable for resolving the oscillation in  $a(x)$ . Thus, the case 5 was computed repeatedly for  $k = 1, 2, 3$  with the same 6-hop extension and tolerance  $\epsilon = 1e-2$ . The local bases were computed by explicitly constructing the weighted  $\mathbf{Z}_i$  and their SVDs. The reduction errors were  $6.5e-5$ ,  $2.0e-5$  and  $6.3e-6$ , respectively.



(a) Wall clock time of computing  $R_{BB,i}$  in seconds.



(b) Wall clock time of computing  $Q_i$  in seconds.

Figure 6: Scaling of local subproblems plotted on log-log scale with degrees-of-freedom on the  $x$ -axis and wall clock time in seconds on the  $y$ -axis. Our optimizations make computing both  $R_{BB,i}$  and  $Q_i$  sub-quadratic.

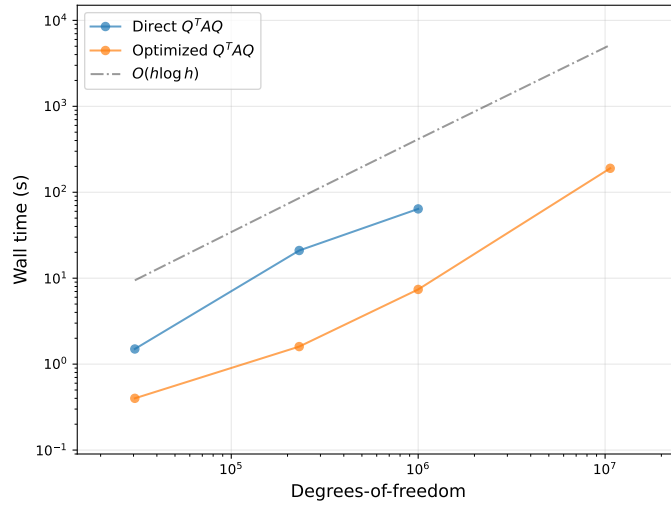


Figure 7: Scaling of  $Q^T A Q$  in seconds of wall clock time on log-log scale. The straight-forward transformation of the system to the reduced basis runs out of memory already in some millions of DOF, while our optimized approach is a magnitude faster and can project problems of almost 100 million DOF.

The  $H^1$  norm of the solution is proportional to the reciprocal of  $a$ , which decreases the upper bound in theorem 5.4. This could explain the decrease in reduction error for higher  $k$ . These preliminary results suggest that the proposed dimension reduction method is not particularly sensitive to large variations in the material parameter.

#### 7.4. Engineering geometry

Many engineering geometries are to some extent "2.5-dimensional" in the sense that the interfaces between the subdomains can be greatly reduced in size through the use of fill-reducing graph partitionings. Smaller interface sizes are expected to further boost the performance of the method, i.e. lead to smaller optimal reduced bases. Thus, as a final example, we present results using a propeller geometry from [18] and the loading

$$f = f(x, y) = x^2 + y^2.$$

Note that the axis  $x = y = 0$  corresponds to the rotational axle of the propeller.

Using Gmsh [12], we created a tetrahedral mesh with 850 558 nodes and 4 394 546 elements. The geometry and the results of the basis reduction are depicted in fig. 8. The results show that for close to half of the 400 subdomains, the subdomains at the propeller blades which originally contain more than a thousand DOFs, are reduced by two orders of magnitude to roughly ten or less DOFs when using 6-hop extensions and the same tolerance as in the scaling test,  $\varepsilon = 1e-2$ , see the graph (c) in fig. 8. Consequently, the system matrix is reduced from  $850\,558 \times 850\,558$  to  $10\,561 \times 10\,561$  which corresponds to a reduction of 98.8% of the DOFs. Note that the case 7 in the scaling tests results in a reduction of 96.5% from  $1\,000\,000 \times 1\,000\,000$  to  $35\,041 \times 35\,041$ , so roughly three times less reduction.

## 8. Conclusions and future work

Model order reduction for finite element methods based on local approximation spaces have been the focus of several papers in recent years, but its potential for distributed computing is yet to be realized. As a step forward, we have extended the numerical analysis of the local approximation problems in terms of weighted  $\ell_2$  norms and derived straightforward error bounds. Consequently, the numerical error becomes simple to control using

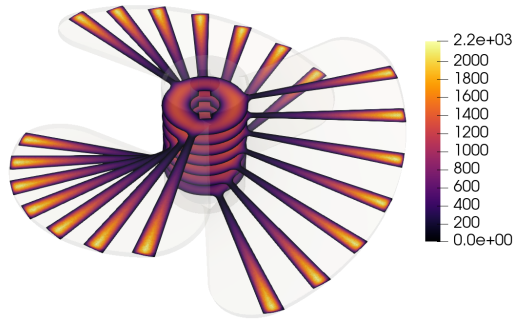
a single parameter,  $\varepsilon > 0$ , interpreted as the tolerance for the worst case reduction error in the  $H^1$  norm. Furthermore, our work has clarified various practicalities of implementing such schemes in a massively parallel computing environment. As the computing nodes do not communicate during the model order reduction, the public cloud becomes a viable compute resource for the method.

The numerical experiments were implemented in the cloud, and included arbitrary mesh partitions and an approach for transforming the global system efficiently using neighboring subdomain information. The results displayed accuracy and conditioning properties that can be expected from an implementation of the piecewise linear finite element method. The reduction error concentrated on the partition interfaces with near-perfect approximations inside the subdomains. The high memory utilization of the graph partitioning algorithm seems to be the first serious bottleneck when scaling up the problem size.

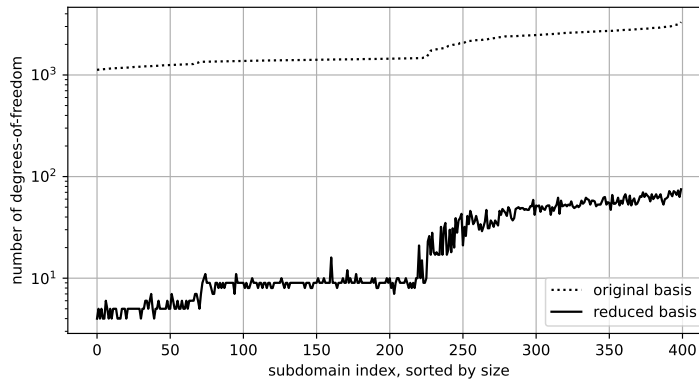
Future work includes extending the analysis to more general partial differential equations and studying alternative approaches for combining the reduced bases over the subdomain interfaces. The latter topic could both generalize the method to higher order finite element methods and improve the partition-of-unity style error estimate to avoid the  $h^{-1}$  scaling. The scheme could also be tested for even larger problems, potentially utilizing accelerator hardware.



(a) A visualization of  $\omega_0$  and the subdomain boundaries.



(b) The reduced solution at a selection of propeller cross sections.



(c) The magnitude of the basis reduction for each subdomain and  $\varepsilon = 1e-2$  on a logarithmic scale.

Figure 8: The results of the engineering geometry example. The blades of the propeller are "2.5-dimensional" with a small constant number of elements ( $\sim 10$ ) in the thickness direction of the blades.

## Appendix A. Proof to lemma 4.2

*Proof.* The squared trace norm can be written as

$$\begin{aligned}
\|z\|_{\partial V_i^+}^2 &= \inf_{\substack{v \in V_i^+, \\ v|_{\partial\omega_i^+ \setminus \partial\Omega} = z}} \|v\|_{1,\omega_i^+}^2 \\
&= \inf_{\substack{v \in V_i^+, \\ v|_{\partial\omega_i^+ \setminus \partial\Omega} = z}} \|v\|_{0,\omega_i^+}^2 + \|\nabla v\|_{0,\omega_i^+}^2 \\
&= \min_{\substack{\beta \in \mathbb{R}^{N_i+M_i}, \\ \beta_B = \beta_z}} \beta^T \mathbf{B}_i^+ \beta + \beta^T \mathbf{A}_i^+ \beta \\
&= \inf_{\substack{\beta \in \mathbb{R}^{N_i+M_i}, \\ \beta_B = \beta_z}} \begin{pmatrix} \beta_I \\ \beta_z \end{pmatrix}^T \begin{pmatrix} \mathbf{A}_{II} & \mathbf{A}_{IB} \\ \mathbf{A}_{BI} & \mathbf{A}_{BB} \end{pmatrix} \begin{pmatrix} \beta_I \\ \beta_z \end{pmatrix},
\end{aligned}$$

where  $\beta$  is the coefficient vector of  $v$  and its boundary indices are constrained to  $\beta_z$ . Because  $\mathbf{B}_i^+$  is symmetric PD and  $\mathbf{A}_i^+$  symmetric PSD,  $\mathbf{A}$  is symmetric PD. The optimization problem can then be solved uniquely by differentiating with respect to  $\beta_I$  and setting the derivative to zero:

$$\begin{aligned}
\nabla_{\beta_I}(\beta^T \mathbf{A} \beta) &= \nabla_{\beta_I}(\beta_I^T \mathbf{A}_{II} \beta_I + 2\beta_I^T \mathbf{A}_{IB} \beta_z + \beta_z^T \mathbf{A}_{BB} \beta_z) \\
&= 2\mathbf{A}_{II} \beta_I + 2\mathbf{A}_{IB} \beta_z \\
&= 0 \\
\implies \beta_I &= -\mathbf{A}_{II}^{-1} \mathbf{A}_{IB} \beta_z.
\end{aligned}$$

Substituting and using lemma 4.1 we get

$$\begin{aligned}
\|z\|_{\partial V_i^+}^2 &= \min_{\beta_I \in \mathbb{R}^{N_i}} \beta_I^T \mathbf{A}_{II} \beta_I + 2\beta_I^T \mathbf{A}_{IB} \beta_z + \beta_z^T \mathbf{A}_{BB} \beta_z \\
&= \beta_z^T \mathbf{A}_{BI} \mathbf{A}_{II}^{-1} \mathbf{A}_{IB} \beta_z - 2\beta_z^T \mathbf{A}_{BI} \mathbf{A}_{II}^{-1} \mathbf{A}_{IB} \beta_z + \beta_z^T \mathbf{A}_{BB} \beta_z \\
&= \beta_z^T (\mathbf{A}_{BB} - \mathbf{A}_{BI} \mathbf{A}_{II}^{-1} \mathbf{A}_{IB}) \beta_z \\
&= \beta_z^T \mathbf{R}_{BB}^T \mathbf{R}_{BB} \beta_z \\
&= \|\mathbf{R}_{BB} \beta_z\|_{\ell_2}^2,
\end{aligned}$$

and taking square roots finishes the proof.  $\square$

## Appendix B. Probabilistic error bound for the low-rank approximation

Per [14, Theorem 10.6], the expected error of the randomized low-rank approximation is

**Lemma Appendix B.1.** *Let  $\mathbf{A} \in \mathbb{R}^{m \times n}$  with singular values  $\sigma_1 \geq \sigma_2 \geq \dots$ . Choose a target rank  $k \geq 2$  and an oversampling parameter  $p \geq 2$ , where  $k + p \leq \min\{m, n\}$ . Draw a standard Gaussian matrix  $\mathbf{\Omega} \in \mathbb{R}^{n \times (k+p)}$  and construct the sample matrix  $\mathbf{Y} = \mathbf{A}\mathbf{\Omega}$ . Then the expected approximation error is*

$$\mathbb{E}\|(\mathbf{I} - \mathbf{P}_Y)\mathbf{A}\|_{\ell_2} \leq \left(1 + \sqrt{\frac{k}{p-1}}\right) \sigma_{k+1} + \frac{e\sqrt{k+p}}{p} (\sum_{j>k} \sigma_j^2)^{1/2}.$$

We also include the tail error result [14, Theorem 10.8].

**Lemma Appendix B.2.** *Consider the assumptions of lemma Appendix B.1. Assume further that  $p \geq 4$ . For all  $u, t \geq 1$ ,*

$$\|(\mathbf{I} - \mathbf{P}_Y)\mathbf{A}\|_{\ell_2} \leq \left(1 + t \cdot \sqrt{\frac{3k}{p+1}}\right) \sigma_{k+1} + t \cdot \frac{e\sqrt{k+p}}{p+1} (\sum_{j>k} \sigma_j^2)^{1/2} + ut \cdot \frac{e\sqrt{k+p}}{p+1} \sigma_{k+1},$$

with failure probability at most  $2t^{-p} + e^{-u^2/2}$ .

For our example at the end of section 7.1, the 6-hop case of fig. C.9 (A) with the sketching parameter  $k_i = \lfloor M_i/8 \rfloor$ , the minimum rank is  $k \approx 40$  and oversampling parameter  $p \approx 175 - k = 135$ . The expected error bound for sketching would then be approximately

$$\frac{3}{2} \sigma_{k+1} + \frac{1}{4} (\sum_{j>k} \sigma_j^2)^{1/2}$$

and the tail error bound with  $t = 2, u = 5$  approximately

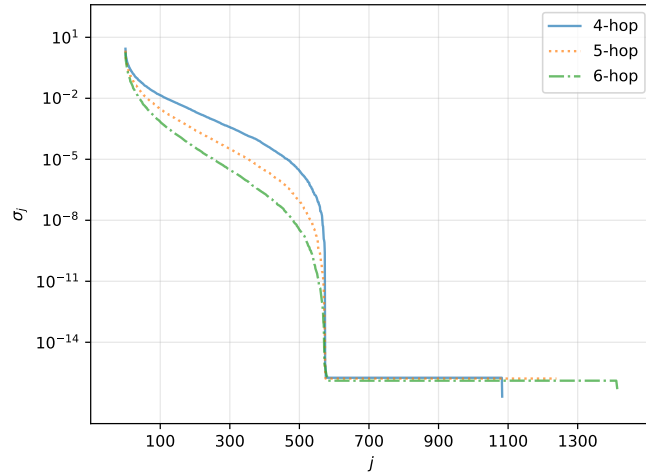
$$\frac{11}{2} \sigma_{k+1} + \frac{1}{2} (\sum_{j>k} \sigma_j^2)^{1/2}$$

with failure probability roughly  $4e-6$ .

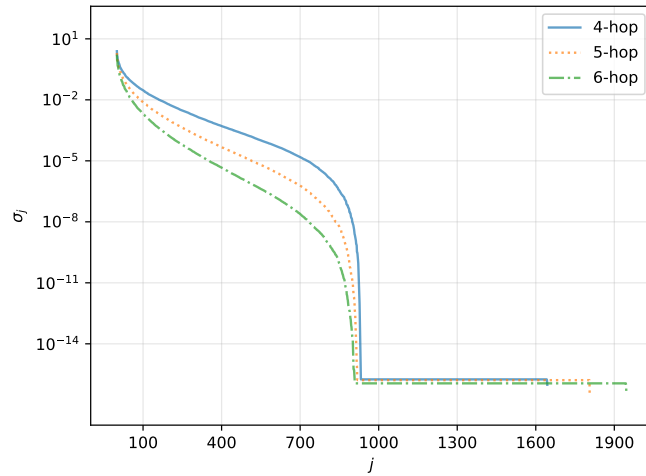
Again, we iterate that while these are the error bounds for the low-rank approximation, the local error bound derived from the low-rank approximation in lemma 5.1 is very loose. Hence, the actual reduction errors present in section 7 are magnitudes smaller.

## Appendix C. Spectra of weighted $\mathbf{Z}_i$

Figure C.9 presents singular values of weighted lifting operators  $\mathbf{Z}_i$  corresponding to two differently sized subdomains and different extensions plotted with a logarithmic  $y$ -axis. Recall that the lifting operator is defined via problem 3.3 and is load-independent. The decay is first exponential, then closer to polynomial, and then again exponential. Noticeably, increased extensions escalate the decay rate, but the singular values go ultimately to machine epsilon at the same number of singular vectors regardless of the extension size. This number is very close to the degrees-of-freedom of the original interface of the subdomain. Intuitively, all solution information of a zero load problem in the subdomain is encoded in the interface degrees-of-freedom, and the weighted  $\mathbf{Z}_i$  closely represents this phenomenon. The original subdomain size does not seem to really affect the rate of decay given the same relative extension. Smaller extensions would result in easier local problems at a cost of slightly more difficult global problems as more boundary dimensions must be included in the approximation. For extensions that roughly double the subdomain diameter, like 6-hop in fig. C.9, using  $k_i = \lfloor M_i/8 \rfloor$  as the sketching parameter seems suitable for yielding optimal bases with tolerance  $\epsilon = 1e-2$  with a very high probability.



(a)  $\#\omega = 2519$  with extensions containing 6 170–9 283 DOFs



(b)  $\#\omega = 4895$  with extensions containing 11 875–17 148 DOFs

Figure C.9: The sorted singular values of weighted  $\mathbf{Z}_i$  for two subdomains with 4, 5 and 6-hop extensions plotted on a logarithmic  $y$ -axis.

## References

- [1] Ivo Babuska and Robert Lipton. Optimal Local Approximation Spaces for Generalized Finite Element Methods with Application to Multiscale Problems. *Multiscale Modeling & Simulation*, 9(1):373–406, January 2011.
- [2] I. Babuška and J. M. Melenk. The Partition of Unity Method. *International Journal for Numerical Methods in Engineering*, 40(4):727–758, 1997.
- [3] Ivo Babuška, Xu Huang, and Robert Lipton. Machine Computation Using the Exponentially Convergent Multiscale Spectral Generalized Finite Element Method. *ESAIM: Mathematical Modelling and Numerical Analysis*, 48(2):493–515, March 2014.
- [4] Ivo Babuška, Robert Lipton, Paul Sinz, and Michael Stuebner. Multiscale-Spectral GFEM and optimal oversampling. *Computer Methods in Applied Mechanics and Engineering*, 364:112960, June 2020.
- [5] Susanne C. Brenner and L. Ridgway Scott. *The Mathematical Theory of Finite Element Methods*, volume 15 of *Texts in Applied Mathematics*. Springer, New York, NY, 2008.
- [6] Andreas Buhr and Kathrin Smetana. Randomized Local Model Order Reduction. *SIAM Journal on Scientific Computing*, 40(4):A2120–A2151, January 2018.
- [7] Victor M. Calo, Yalchin Efendiev, Juan Galvis, and Guanglian Li. Randomized Oversampling for Generalized Multiscale Finite Element Methods. *Multiscale Modeling & Simulation*, 14(1):482–501, January 2016.
- [8] Susan Coghlan. The Magellan Final Report on Cloud Computing. December 2011.
- [9] Victorita Dolean, Pierre Jolivet, and Frédéric Nataf. *An Introduction to Domain Decomposition Methods: Algorithms, Theory, and Parallel Implementation*. Society for Industrial and Applied Mathematics, Philadelphia, PA, November 2015.

- [10] Yalchin Efendiev, Juan Galvis, and Thomas Y. Hou. Generalized multiscale finite element methods (GMsFEM). *Journal of computational physics*, 251:116–135, 2013.
- [11] Yalchin Efendiev, Juan Galvis, Guanglian Li, and Michael Presho. Generalized multiscale finite element methods: Oversampling strategies. *International Journal for Multiscale Computational Engineering*, 12(6), 2014.
- [12] Christophe Geuzaine and Jean-François Remacle. Gmsh: A 3-D finite element mesh generator with built-in pre- and post-processing facilities. *International Journal for Numerical Methods in Engineering*, 79(11):1309–1331, September 2009.
- [13] Tom Gustafsson and G. D. McBain. scikit-fem: A Python package for finite element assembly. *Journal of Open Source Software*, 5(52):2369, August 2020.
- [14] N. Halko, P. G. Martinsson, and J. A. Tropp. Finding Structure with Randomness: Probabilistic Algorithms for Constructing Approximate Matrix Decompositions. *SIAM Review*, 53(2):217–288, January 2011.
- [15] Antti Hannukainen, Jarmo Malinen, and Antti Ojalampi. Distributed Solution of Laplacian Eigenvalue Problems. *SIAM Journal on Numerical Analysis*, 60(1):76–103, February 2022.
- [16] George Karypis and Vipin Kumar. METIS: A Software Package for Partitioning Unstructured Graphs, Partitioning Meshes, and Computing Fill-Reducing Orderings of Sparse Matrices. Report, 1997.
- [17] Vili Kohonen and Tom Gustafsson. Numerical experiments for "Distributed finite element solution using model order reduction", April 2024.
- [18] Franck Ledoux. MAMBO-project: Model database mesh blocking.
- [19] Chupeng Ma and Robert Scheichl. Error estimates for discrete generalized FEMs with locally optimal spectral approximations. *Mathematics of Computation*, 91(338):2539–2569, 2022.

- [20] Chupeng Ma, Robert Scheichl, and Tim Dodwell. Novel Design and Analysis of Generalized Finite Element Methods Based on Locally Optimal Spectral Approximations. *SIAM Journal on Numerical Analysis*, 60(1):244–273, February 2022.
- [21] Per-Gunnar Martinsson and Joel A. Tropp. Randomized numerical linear algebra: Foundations and algorithms. *Acta Numerica*, 29:403–572, 2020.
- [22] Vanderlei Munhoz, Márcio Castro, and Odorico Mendizabal. Strategies for fault-tolerant tightly-coupled HPC workloads running on low-budget spot cloud infrastructures. In *2022 IEEE 34th International Symposium on Computer Architecture and High Performance Computing (SBAC-PAD)*, pages 263–272, 2022.
- [23] François Pellegrini and Jean Roman. Scotch: A software package for static mapping by dual recursive bipartitioning of process and architecture graphs. In Heather Liddell, Adrian Colbrook, Bob Hertzberger, and Peter Sloot, editors, *High-Performance Computing and Networking*, Lecture Notes in Computer Science, pages 493–498, Berlin, Heidelberg, 1996. Springer.
- [24] Jr. Roy Craig. Coupling of substructures for dynamic analyses - An overview. In *41st Structures, Structural Dynamics, and Materials Conference and Exhibit*. American Institute of Aeronautics and Astronautics.
- [25] Julia Schleuß and Kathrin Smetana. Optimal Local Approximation Spaces for Parabolic Problems. *Multiscale Modeling & Simulation*, 20(1):551–582, March 2022.
- [26] Andrea Toselli and Olof B. Widlund. *Domain Decomposition Methods — Algorithms and Theory*, volume 34 of *Springer Series in Computational Mathematics*. Springer, Berlin, Heidelberg, 2005.
- [27] Rüdiger Verfürth. *A Posteriori Error Estimation Techniques for Finite Element Methods*. Oxford University Press, April 2013.
- [28] Barbara I. Wohlmuth. *Discretization Methods and Iterative Solvers Based on Domain Decomposition*, volume 17 of *Lecture Notes in Com-*

*putational Science and Engineering*. Springer Berlin Heidelberg, Berlin, Heidelberg, 2001.

- [29] Jiazheng Zhou, Xuan-Yi Lin, and Yeh-Ching Chung. Hardware supported multicast in fat-tree-based InfiniBand networks. *The Journal of Supercomputing*, 40(3):333–352, June 2007.